Radarcoding Reference Data for SAR Training Data Creation in Radar Coordinates

Anurag Kulshrestha, *Member, IEEE*, Ling Chang, and Alfred Stein

***Abstract*— Extracting training datasets for supervised classification of synthetic aperture radar (SAR) images is complicated, due to, e.g., poor radiometric resolution, speckle noise, and lack of reference data. It is challenging to link radar scatterers in SAR images with the counterparts in the reference datasets registered in geographic coordinate systems. To address this issue, this letter proposes a method called Rdr-Code to radarcode geodetic reference datasets for creating SAR training datasets for machine learning applications. To assess the importance of building heights in radarcoding, we compared the assignment of height values by a minuscule pseudo height with the actual building heights derived from a Lidar-based DEM product. We used 30 PAZ SAR images in X-band, which were acquired between 2019 and 2021, over the north-west part of the Netherlands, and employed Top10NL and AHN as reference LULC polygon and height datasets, respectively. The radarcoding accuracy was compared using nine buildings as references in the SAR coordinates. The radarcoding accuracy was 64.5% with the pseudo height and 84.5% with actual building heights. A trade-off between accurate building feature information and separation between close buildings was observed. We conclude that this is an effective way to radarcode reference datasets and can be used for crafting training datasets for machine learning methods.**

***Index Terms*— AHN, radarcoding, supervised classification, synthetic aperture radar (SAR), Top10NL, training data.**

I. Introduction

SYNTHETIC aperture radar (SAR) datasets are useful in classifying ground targets [1], scattering mechanisms [2], as well as for identifying the movement of ground objects in interferometric phase images [3]. SAR-based classification using supervised algorithms, especially 'data-hungry' deep learning methods [4], requires training datasets. In the absence of benchmark labeled datasets for SAR data, one often turns to self-delineation of these datasets. The creation of these training datasets can be a time-intensive and demanding task. As SAR datasets are usually referenced to their relative radar coordinate system, one option is first to flip, shift, and stretch the single-look complex (SLC) or multilook complex (MLC) images with respect to the geographic coordinate system, and then label SAR training datasets by visual interpretation and comparison with optical observations. This, however, makes it cumbersome to identify targets and increases the chance of introducing bias in the training datasets. Another option is to use georectified ground range detected (GRD) products of, e.g., Sentinel-1 SAR mission [5]. GRD datasets, however, merely provide amplitude-related features, like backscatter coefficients, and not phase-related features. This hinders the extraction of several polarimetric features, such as the copolarization cross-product: $S_{hh} \cdot S_{vv}^{*}$, and the copolarization phase difference: $\psi_{hh} - \psi_{vv}$ (S_{hh}, S_{vv}, are the complex elements of scattering matrix in HH and VV polarization channels, and ψ_{hh} and ψ_{vv} are the SLC phases in these respective polarizations). There have been a few attempts made for coding radar datasets, but they have been mostly carried out for large areas, e.g., in mountainous areas, and they have mostly focused on geocoding radar datasets in WGS coordinates, e.g., [6]. Radarcoding was also used to classify radar scattering mechanisms using PAZ data [7]. In this study, we present the strategy for radarcoding available labeled datasets from geographic coordinates to radar coordinates and use them to create unbiased training datasets.

In the remaining part of this letter, we first review the theory behind radarcoding in Section II, then move toward explaining the methodology in Section III. Section IV shows the application of the method using PAZ SAR datasets, available labeled reference datasets, e.g., Top10NL with land use and land cover (LULC) and actual height of Netherlands (AHN) information, and software tools such as GDAL [8] and DORIS [9]. We also discuss the results in Section V, and finally conclude in Section VI.

II. Radarcoding Theory

Reference datasets are usually rasterized and referenced to the geographical coordinates, e.g., WGS84 coordinates. A radar-coded grid can then be constructed by following a two-step procedure [10]. Step 1: the geographical coordinates including latitude (ϕ), longitude (λ), and ellipsoidal height (h), are converted into geocentric Cartesian coordinates, with x, y, z using the known parameters of, e.g., WGS84 ellipsoid. These Cartesian coordinates are obtained as

$$\begin{aligned} x &= (N+h)\cos(\phi)\cos(\lambda) \\ y &= (N+h)\cos(\phi)\sin(\lambda) \\ z &= ((1-e^2)N+h)\sin(\lambda) \end{aligned} \tag{1}$$

where N is the radius of curvature in the prime vertical, obtained as $N = ell_a/(1-e^2\sin^2(\phi))^{1/2}$, while $e^2 = (ell_a^2 - ell_b^2)/ell_a^2$ is the squared first eccentricity of the WGS reference ellipsoid, and ell_a and ell_b are its semimajor and semiminor axes, respectively.

Manuscript received 13 July 2023; revised 3 January 2024; accepted 17 January 2024. Date of publication 22 March 2024; date of current version 27 March 2024. This work was supported by European Space Agency (ESA) for Funding Open SAR Library under Grant 4000140600/23/I-DT. *(Corresponding author: Anurag Kulshrestha.)*

The authors are with the Department of Earth Observation Science, Faculty of Geoinformation Science and Earth Observation (ITC), University of Twente, 7500 AE Enschede, The Netherlands (e-mail: a.kulshrestha@utwente.nl; ling.chang@utwente.nl; a.stein@utwente.nl).

Digital Object Identifier 10.1109/LGRS.2024.3376992

TABLE I
SAMPLE POSITIONAL VECTORS FOR SATELLITE ORBITS. HERE, THE SUBSCRIPTS 0, n DEPICT THE EARLIEST AND LATEST MEASUREMENTS

Time	x	y	z
t_0	x_0	y_0	z_0
$\vdots$	$\vdots$	$\vdots$	$\vdots$
t_n	x_n	y_n	z_n

Step 2: The Cartesian coordinates are converted into radar coordinates with azimuth (az, with lines) and range (rg, with pixels) direction. To do so, the preliminary orbits are first gathered from the product metadata, e.g., through the Sentinel-1 orbit data portal [11], or from the metadata XML files provided with the datasets for, e.g., TerraSAR-X and PAZ. They can be arranged as shown in Table I.

During this Step 2, the time t is normalized using between earliest and latest time points, i.e., t_0 and t_n, respectively, using $t_{norm} = (t - t_0)/(t_n - t_0)$. Along with positional coordinates in Table I, the normalized time is used to fit the positional vectors in each spatial dimension r with $r \in \{\mathbf{x}, \mathbf{y}, \mathbf{z}\}$ using a quadratic function at time t: $r|_t = a_r t^2 + b_r t + c_r$. After estimating the parameters in this function, they are rescaled with respect to the actual time using

$$(a_r, b_r, c_r) \leftarrow \left(\frac{a_r}{(t_n - t_0)^2}, \frac{b_r}{(t_n - t_0)} - \frac{2a_r t_0}{(t_n - t_0)^2}, c_r - \frac{b_r t_0}{(t_n - t_0)} + \frac{a_r t_0^2}{(t_n - t_0)^2} \right). \tag{2}$$

Using the quadratic model, the instantaneous velocities and accelerations are derived as $v_r = \partial r(t)/\partial t$ and $a_r = \partial^2 r(t)/\partial t^2$. Thereafter, the positional, velocity, and acceleration vectors are interpolated with respect to the time t_{l_m} associated with the midline (l_m) of the acquired image, where $t_{l_m} = ((l_m - 1)/PRF) + t_{l_0}$. Here, PRF is the pulse repetition frequency and t_{l_0} is the time corresponding to the first line. These can be read as

$$\begin{aligned} v_r|_{t_{l_m}} &= 2a_r t_{l_m} + b_r \\ a_r|_{t_{l_m}} &= 2a_r \end{aligned} \tag{3}$$

where the symbol $|_{t_{l_m}}$ suggests the interpolation at t_{l_m}. Following this, we estimate the time associated with Cartesian coordinates (from Step 1) with respect to the mid-azimuth line. For each time point, the distance between the actual position and the interpolated position with respect to t_{l_m}, i.e., $\Delta_r = r - r|_{t_{l_m}}$ is estimated. This is used in turn to estimate the time difference as

$$\Delta t = \frac{-\sum_{r\in\{x,y,z\}} (v_r|_{t_{l_m}} \cdot \Delta_r)}{\sum_{r\in\{x,y,z\}} (a_r|_{t_{l_m}} \cdot \Delta_r) - \sum_{r\in\{x,y,z\}} (v_r|_{t_{l_m}})^2} \tag{4}$$

where summation is over all the three spatial dimensions, i.e., $r \in \{x, y, z\}$. Using Δt, the time t_{l_m} is adjusted as $t_{l_m} \leftarrow t_{l_m} + \Delta t$. This readjustment is done iteratively until Δt converges to zero or until the maximum number of iterations is reached. This final value of the parameter t_{l_m}, is then assigned as the azimuth time (t_{az}) associated with the Cartesian coordinates. This process is repeated for all (x, y, z) derived from Step 1.

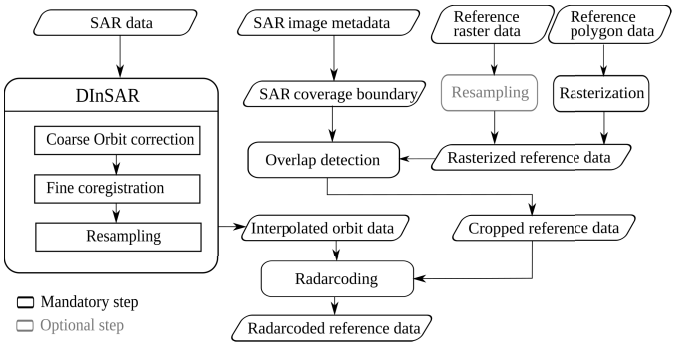

Fig. 1. Methodological flow diagram.

The range time t_{rg} is estimated as

$$t_{rg} = \frac{\sqrt{\sum_{r\in\{x,y,z\}} \Delta_r^2}}{c} \tag{5}$$

where c is the speed of light. Then, the radar line numbers l and pixel numbers p are estimated as

$$\begin{aligned} l &= 1 + \mathrm{PRF}(t_{ag} - t_{l_0}) \\ p &= 1 + 2 \cdot \mathrm{RSR}(t_{rg} - t_{r_0}) \end{aligned} \tag{6}$$

where RSR is the range sampling rate and t_{r_0} is the range time associated with the first column of the radar image.

After estimating the geometry of the grid, the feature values are radiometrically interpolated into the grid, e.g., using bilinear convolution. In this way, the radarcoding of the reference datasets is completed. This method is based on the radarcoding implementation in the Doris software [9].

III. METHODS

The practical methodology is illustrated in the methodological flow diagram Fig. 1. At least two repeat-pass SAR images, namely master and slave SAR image, are processed using differential SAR Interferometry (DInSAR) [12]. The positional vectors for the satellites, as indicated in Table I, are estimated using the coarse orbit estimation step [9]. The orbit points are then interpolated using (2) with the midline timing. Both master and slave images are coregistered to ensure geometrical consistency between the images. The slave image needs to be resampled after coregistration. The midline number, PRF, RSR, first-line timing, and first-pixel timing information are taken from the SAR image metadata. The SAR coverage boundary is extracted using the extreme extent coordinates from the satellite image metadata.

The reference polygon datasets are rasterized classwise using the GDAL rasterize function. Here, the choice of the raster image resolution is dependent upon the size of reference polygons, the spatial resolution of the SAR data, and the processing limitations of the computer. Higher resolutions are better for smooth representations of polygon features in the raster data model, but this can cause the raster dataset to become too fine as compared to the resolution of SAR data or too large in terms of the computer memory space.

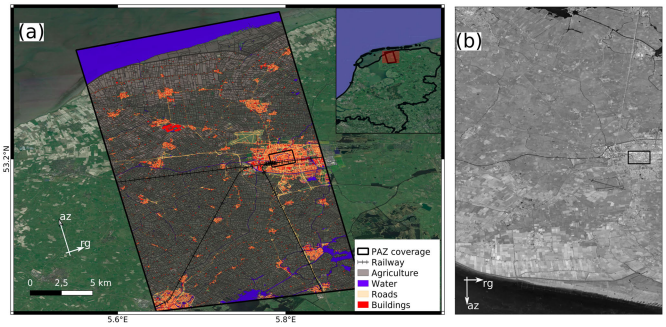

Fig. 2. (a) Study area and (b) PAZ time-averaged intensity image in VV channel ($\bar{I}_{VV}$).

In case the reference datasets are available as rasters, e.g., optical images, generic atmospheric correction online service for InSAR (GACOS) atmospheric phase delay maps [13], and the datasets can be used directly for radarcoding. However, they can be optionally resampled to a required spatial resolution. This is especially required for datasets with ultrafine resolutions.

The pixel values of the rasterized reference datasets are interpreted as geographical heights, and the pixel values are rescaled between 0 and a minuscule positive real number ϵ. These values can be scaled back in the original range after radarcoding. For polygons that are rasterized, the resulting rasters are assigned a value of ϵ to the pixels overlapping the polygons. This is to avoid unwanted layover and foreshadowing effects for flat features, i.e., roads and water. For buildings, we experimented with ϵ and using actual building heights, e.g., AHN [14]. This is done for two reasons. First, to account for the layover and shadow effects of high-rise buildings, and second, to account for different building shapes.

Next, the geographical extent of the reference data and the SAR data coverage are cropped to a common intersecting geometry. The geometry of the cropped reference dataset is then radarcoded using (6) and brought to the same coordinate system as that of the SAR data. Finally, the class values are interpolated into the radarcoded grid.

The radarcoding accuracy is assessed by comparing the radarcoded pixels of nine buildings, with nonuniform shapes or tall heights, with masks drawn using the SAR intensity image. The percentage of areal overlap is considered as the accuracy metric. Note that the whole methodology is developed and implemented upon Doris [9], and scripted in python and available on GitHub with repository name: *rdrcode*.

IV. Application

For the application of our method, we chose a study area over the north-west of the Netherlands, covering large parts of the province Friesland, see Fig. 2(a). The map shows five LULC classes: Buildings, Roads, Water, Agriculture, and Railway line. A set of 30 multitemporal X-band, descending pass, stripmap mode PAZ images in VV was acquired over the extent cropped and marked as 'PAZ coverage' in Fig. 2(a) between 2019-09-28 and 2021-10-15. The time averaged intensity image in VV (denoted as $\bar{I}_{VV}$) corresponding to the master date is shown in Fig. 2(b). Due to the descending pass of the satellite, an upside-down shift can be observed between the two subfigures. The black polygon inside Fig. 2(a) and (b) shows the extent of the crop that is going to be used for further analysis.

Vector datasets for the five LULC classes were acquired from open data portals. The agriculture parcel data were acquired from the Publieke Dienstverlening Op de Kaart (PDOK) [15] while the data for the remaining four classes were acquired using the Top10NL product made available by the Kadaster [16]. The building heights were acquired from the AHN3 [14] data. Next, the vector datasets were cropped to the extent of the satellite image. The cropped vector datasets were then individually rasterized using GDAL to a user-defined spatial resolution. In our case, we chose a resolution equal to 10^{-4} decimal degrees or approximately 11 m. The value of ϵ was 0.1 m. Thereafter, the rasterized files were radarcoded.

The results after radarcoding are displayed in Fig. 3. Fig. 3(a) shows the crop corresponding to the black polygon in Figs. 2(a) and 3(b) show the radarcoded image with LULC classes. These radarcoded images show an exact match over the radar image. This can be seen in Fig. 3(c) which shows the overlay of the radarcoded reference data over the SAR intensity image. The radarcoded data are vectorized using GDAL using a connectivity of 8 pixels.

Next, we used the AHN data to extract building heights. The extracted building heights were radarcoded and used to create the building footprints. The radarcoded building heights can be seen in Fig. 3(d). Fig. 3(e) shows the radarcoded LULC map, and Fig. 3(f) shows the overlay of vectorized version of Fig. 3(e) on top of SAR amplitude image. For this version, we put a threshold of 3 m as the minimum height for buildings. The image in Fig. 3(e) is slightly darkened for all areas except for the masked building used for radarcoding accuracy assessment.

To compare the results between using a pseudo height ϵ to radarcode building footprints and using actual building heights, we analyzed the histograms of $\bar{I}_{VV}$ values for pixels overlapped by the radarcoded building, roads and water classes. Fig. 4(a) shows the $\bar{I}_{VV}$ distribution of the three classes with polygons radarcoded with height ϵ. As expected, the mode of the building class distribution is the highest, followed by the mode of the road class and the mode of the water class being the lowest. Similarly, Fig. 4(b) shows the distribution of the three classes where building heights are used to radarcode building polygons. The distribution follows a similar trend as in Fig. 4(a), but with reduced peak values for each classes. This reduction in the number of pixels is evident in the difference of the above two histograms as shown in Fig. 4(c). The reduction is highest for the road class followed by the building class. Quantitatively, there was approximately a 4% reduction in the number of building pixels, whereas a 7% reduction in road samples between the histograms shown in Fig. 4(a) and (b). There is also an increase of high $\bar{I}_{VV}$ values for the building class suggesting an increase in the percentage of high intensity scatterers overlapped by the building class.

For further analysis of building shapes, we highlight a set of buildings using a white rectangle in Fig. 3(a), (c), (d), and (f). A zoomed-in version of the figure is shown in Fig. 5. Fig. 5(a) shows a 3-D perspective view of the buildings,

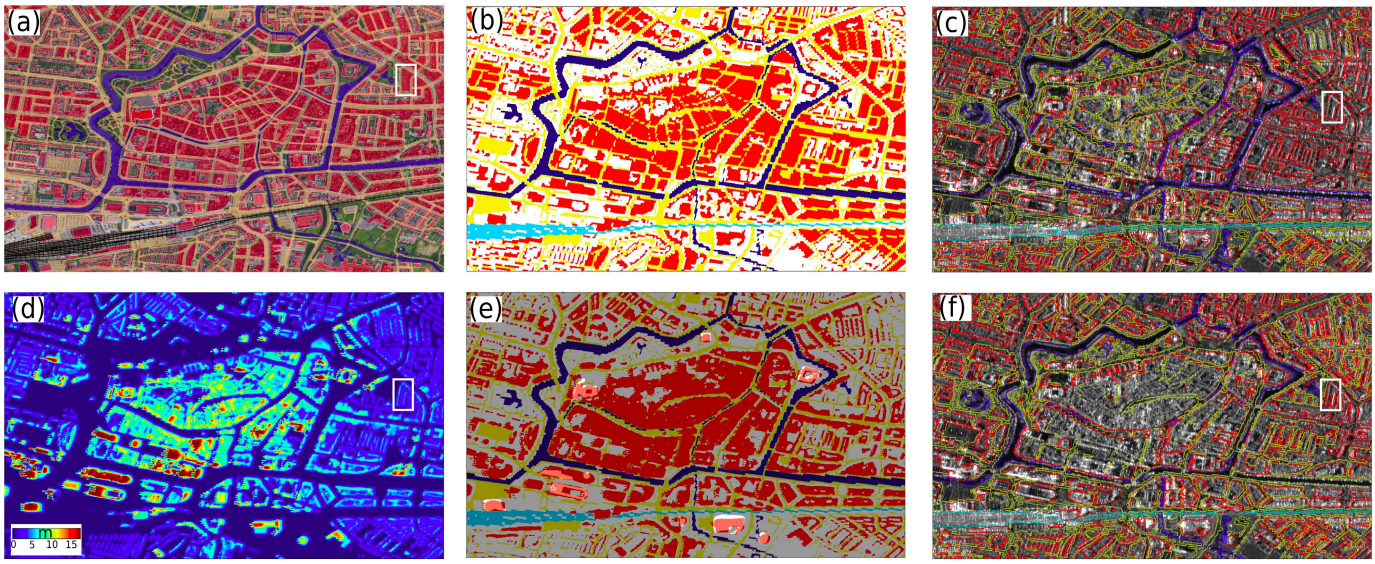

Fig. 3. (a) Crop of reference land cover classes in WGS coordinates corresponding to the city of Leeuwarden, The Netherlands, corresponding to the black rectangle in Fig. 2(a). (b) Shows the radarcoded classes with buildings, roads, water, and railway shown using red, yellow, blue, and cyan colors. (c) Shows an overlay of the radarcoded data over the PAZ amplitude image. (d) Shows the radarcoded building heights. (e) Shows the radarcoded classes using building heights with the masks of building polygons used for accuracy assessment. (f) Shows its corresponding overlap.

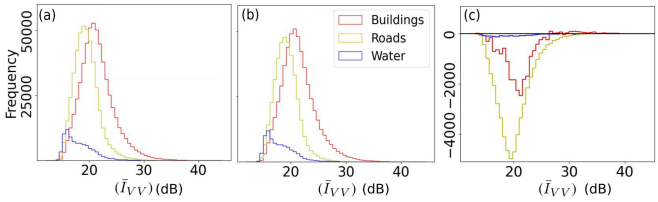

Fig. 4. Histograms of $\bar{I}_{VV}$ overlapped by radarcoded areas for building, roads, and water classes (a) without using building heights, (b) using building heights, and (c) difference between (b) and (a).

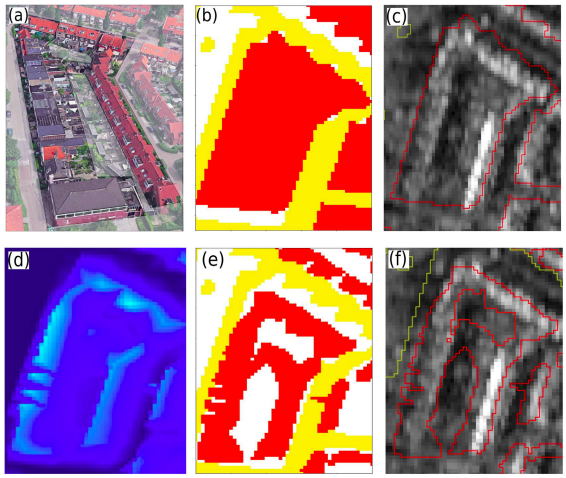

Fig. 5. Zoomed-in image of the building outlined by a white rectangle in Fig 3. The descriptions of sub-figures follow correspondingly as in Fig. 3.

overlaid by a mask that hides the other surrounding buildings. Fig. 5(b) and (c) shows the radarcoded images in raster and vector form, respectively, for standard reference polygons. Fig. 5(d) shows the radarcoded DEM of the buildings. Fig. 5(e) and (f) shows the radarcoded images in raster and vector images with building pixels thresholded by a height of 3 m. Fig. 5(f), shows that the building polygon follows the shape of buildings from the 3-D perspective view in Fig. 5(a), while the building footprint shown in Fig. 5(c) covers the entire building. This results in a reduction of the number of pixels with low-intensity values within the building boundary defined by the reference polygon. These rejected pixels may have similarities with other LULC classes, such as water and roads. This ultimately improves the geographic accuracy and feature reliability of SAR training data.

TABLE II
DISTRIBUTION OF RADARCODED PIXELS OVER BUILDING REFERENCE

Radarcoding Type	Building	Roads	Railway	Water	Mask	Accuracy
Pseudo height	7781	445	55	145	3649	64.43%
Building height	10214	110	8	78	1665	84.59%

The radarcoding accuracy was also assessed. A total of 12 075 pixels overlapped with the nine buildings selected as the reference. These buildings were radarcoded with an overlap accuracy of 64.43% in case of building heights assigned as ϵ. This accuracy increases to 84.59% for buildings assigned with the true heights using the radarcoded DEM. Table II shows the distribution of reference pixels over the four radarcoded classes, and the no-data masked area. An increase in the building class pixels and a reduction in the road class pixels can be observed in the latter case. This indicates a possible encroachment of buildings into the road class.

V. DISCUSSION

The transformation of geometries from WGS coordinates to radar coordinates is more complicated than a simple affine transformation. This is especially because of the slant acquisition geometry of the radar sensor. In this study, we show the application of radarcoding to overlay land use and land cover classes in radar coordinates. The distribution of the radarcoded classes are shown in the histograms in Fig. 4. The reason for the mode to be the highest for the building class and the least for the water class is most likely due to the higher presence of high and low intensity scatterers in the respective cases.

In this study, we experimented with using a pseudo height ϵ versus actual building height to get radarcoded geometries. We clearly observe a trade-off between accurate building feature information and separation between close buildings. In case of using building heights for radarcoding building polygons, we observe that there is an increase in high-intensity pixels overlapped by building polygons. This could most likely be owed to better accounting of layover and foreshortend pixels using the actual building heights. In a few cases, we also observed that the extracted building shapes resemble the building shapes from the optical images. We further observed that the number of road pixels are reduced in the case with building heights. This is mainly due to the resampling of the building heights from a coarse resolution. Since resampling is done from a coarse resolution posting of the height model, it could be responsible for this 'smearing' of buildings in the radarcoded image. A finer resolution of the building heights could reduce this tradeoff.

We achieved a high radarcoding accuracy. The accuracy was assessed for nine buildings with tall heights and nonuniform shapes. Building class was considered to be the best class to assess the overlap accuracy because they are supposed to be the class most impacted by geometrical distortions, such as layover and foreshortening. Other classes, such as roads, were not chosen because it was difficult to delineate polygons over such narrow features in the radar image. The number of testing sites can further be increased to increase the significance of the radarcoding accuracy.

VI. Conclusion

This letter proposed a strategy for obtaining labeled SAR data in radar coordinates using the radarcoding method addressed in Section II. The application in Section IV demonstrated this strategy is useful in extracting labeled SAR datasets for LULC classification.

We identified a trade-off between the building feature accuracy and the separation between buildings in the use of building heights for radarcoding. We recommend using building heights during radarcoding when buildings tall or farther spaced out, so as to reduce the 'smearing' effect of building onto other classes. The radarcoding accuracy was 64.43% with the pseudo height and 84.59% with actual building heights.

In the processing, we recommend that the rasterization and radarcoding be done per class. This helps in dealing with the border pixel values between two or more classes. We further recommend the use of data augmentation to increase the number of training datasets. We can also use novel data augmentation strategies to generate multiscale datasets for learning ground features at various scales. In addition to LULC-related datasets, other available geospatial reference data like meteorological and geological measurements can also be radarcoded. In addition to vector datasets, raster could also be used.

References

[1] Z. Qi, A. G.-O. Yeh, X. Li, and Z. Lin, "A novel algorithm for land use and land cover classification using RADARSAT-2 polarimetric SAR data," *Remote Sens. Environ.*, vol. 118, pp. 21–39, Mar. 2012.

[2] A. Kulshrestha, L. Chang, and A. Stein, "Use of LSTM for sinkhole-related anomaly detection and classification of InSAR deformation time series," *IEEE J. Sel. Topics Appl. Earth Observ. Remote Sens.*, vol. 15, pp. 4559–4570, 2022.

[3] N. Anantrasirichai, J. Biggs, F. Albino, P. Hill, and D. Bull, "Application of machine learning to classification of volcanic deformation in routinely generated InSAR data," *J. Geophys. Res., Solid Earth*, vol. 123, no. 8, pp. 6592–6606, Aug. 2018.

[4] N. I. Bountos, D. Michail, and I. Papoutsis, "Learning from synthetic InSAR with vision transformers: The case of volcanic unrest detection," *IEEE Trans. Geosci. Remote Sens.*, vol. 60, 2022, Art. no. 4509712.

[5] R. Torres et al., "GMES Sentinel-1 mission," *Remote Sens. Environ.*, vol. 120, pp. 9–24, May 2012.

[6] I. Petillot et al., "Radar-coding and geocoding lookup tables for the fusion of GIS and SAR data in mountain areas," *IEEE Geosci. Remote Sens. Lett.*, vol. 7, no. 2, pp. 309–313, Apr. 2010.

[7] L. Chang, A. Kulshrestha, B. Zhang, and X. Zhang, "Extraction and analysis of radar scatterer attributes for PAZ SAR by combining time series InSAR, PolSAR, and land use measurements," *Remote Sens.*, vol. 15, no. 6, p. 1571, Mar. 2023.

[8] GDAL/OGR Contributors. (2020). *GDAL/OGR Geospatial Data Abstraction software Library, Open Source Geospatial Foundation*. [Online]. Available: https://gdal.org

[9] B. M. Kampes and R. F. Hanssen, "Delft object-oriented radar interferometric software: Users manual and technical documentation," Delft Inst. Earth Observ. Space Syst. (DEOS), Delft Univ. Technol., Delft, The Netherlands, Tech. Rep., 2008.

[10] D. Geudtner and M. Schwabisch, "An algorithm for precise reconstruction of InSAR imaging geometry: Application to flat-earth; Phase removal, phase-to-height conversion and geocoding of InSAR-derived DEMs," in *Proc. EUSAR*, 1996. [Online]. Available: https://elib.dlr.de/23829/

[11] ESA. (2022). *Copernicus Sentinels POD Data Hub*. [Online]. Available: https://scihub.copernicus.eu/gnss

[12] A. Moreira, P. Prats-Iraola, M. Younis, G. Krieger, I. Hajnsek, and K. P. Papathanassiou, "A tutorial on synthetic aperture radar," *IEEE Geosci. Remote Sens. Mag.*, vol. 1, no. 1, pp. 6–43, Mar. 2013.

[13] C. Yu, Z. Li, N. T. Penna, and P. Crippa, "Generic atmospheric correction model for interferometric synthetic aperture radar observations," *J. Geophys. Res., Solid Earth*, vol. 123, no. 10, pp. 9202–9222, Oct. 2018.

[14] AHN. (2023). *Actueel Hoogtebestand Nederland*. Accessed: Jan. 26, 2023. [Online]. Available: www.ahn.nl

[15] PDOK. (2023). *Publieke Dienstverlening Op de Kaar*. [Online]. Available: https://www.pdok.nl

[16] Kadaster. (2023). *Kadaster*. [Online]. Available: https://www.kadaster.nl